JOURNAL OF SPACECRAFT AND ROCKETS
Vol. 50, No. 2, March–April 2013

Trajectory Estimation of the Hayabusa Spacecraft During Atmospheric Disintegration

Michael A. Shoemaker*
Kyushu University, Fukuoka 819-0395, Japan
Jozef C. van der Ha†
Mission Design and Operations, Deming, Washington 98244
Shinsuke Abe‡
National Central University, Taoyuan 32001, Taiwan, Republic of China
and
Kazuhisa Fujita§
Japan Aerospace Exploration Agency, Kanagawa 229-8510, Japan

DOI: 10.2514/1.A32338

The Hayabusa spacecraft was intentionally destroyed in the atmosphere at superorbital velocity at the conclusion of its asteroid sample return mission in June 2010. This study uses single-station ground-based video observations of the reentry to analyze the breakup of the spacecraft and estimate the trajectory of 80 individual spacecraft fragments. An extended Kalman filter with batch initialization is used to estimate the position, velocity, and aerodynamic ballistic coefficients of the fragments. The breakup is characterized and compared with preflight predictions. A high area-to-mass object is seen early during the reentry, which matches closely with the predicted solar panel separation. Nearly all fragments have decreasing freestream dynamic pressure during their observed trajectories. Fragments with high drag ballistic coefficients are more likely to be observed early in the reentry. Assuming simple aluminum spheres, the estimated ballistic coefficients show that the fragments would have radius and mass on the order of centimeters and grams, respectively. The ablation coefficient is also calculated for several fragments using the estimated velocities and ballistic coefficients; results resemble natural meteors and agree with other studies of the Hayabusa reentry using different methods.

Nomenclature

$\mathbf{A}$	=	state Jacobian matrix
$\mathbf{a}$	=	acceleration vector, m/s^2
C	=	coefficient
$\mathcal{C}$	=	observation matrix for initial state estimate
$\mathbf{C}^{it}$	=	rotation matrix from $\mathcal{F}_t$ to $\mathcal{F}_i$
$\mathbf{c}$	=	sensor position vector from Earth's center, m
$E(\cdot)$	=	expectation operator
$\mathbf{F}$	=	system dynamics model vector
$\mathcal{F}$	=	reference frame
$\mathbf{G}$	=	measurement model vector
$\mathbf{H}$	=	measurement Jacobian matrix
H	=	scale height, m
h_{ellp}	=	altitude above Earth's ellipsoid, m
h_0	=	reference altitude, m
I	=	luminosity, W
J	=	number of measurements to estimate initial state
$\mathbf{K}$	=	Kalman gain matrix
K	=	number of filter measurements
L	=	number of batch measurements
M	=	number of root-mean-square measurements
m	=	mass, kg
$\hat{\mathbf{n}}$	=	reference plane unit normal
$\mathbf{P}$	=	state estimate error covariance matrix
$\mathbf{Q}$	=	spectral density of process noise matrix
$\mathbf{q}$	=	system process noise vector
$\mathbf{R}$	=	measurement noise covariance matrix
R_e	=	Earth's equatorial radius, m
R_p	=	Earth's polar radius, m
$\mathbf{r}$	=	target position vector from Earth's center, m
S	=	reference area, m^2
$\mathbf{t}_{1i}$	=	$\mathcal{F}_t$ one-axis unit vector in $\mathcal{F}_i$
$\mathbf{t}_{2i}$	=	$\mathcal{F}_t$ two-axis unit vector in $\mathcal{F}_i$
$\mathbf{t}_{3i}$	=	$\mathcal{F}_t$ three-axis unit vector in $\mathcal{F}_i$
$\mathbf{v}$	=	inertial velocity vector, m/s
$\mathbf{v}_{\text{er}}$	=	Earth-relative velocity vector, m/s
$\mathbf{X}$	=	state vector
$\mathbf{x}$	=	state deviation vector
$\mathbf{Y}$	=	measurement vector
$\mathcal{Y}$	=	initialization measurement vector
$\mathbf{y}$	=	measurement residual vector
β	=	ballistic coefficient, m^2/kg
ϵ	=	measurement noise
μ	=	Earth's gravitational parameter, m^3/s^2
ξ	=	heat of ablation per unit mass, m^2/s^2
ρ	=	range vector from sensor to target, m
$\hat{\rho}$	=	unit line-of-sight vector
ρ	=	atmospheric density, kg/m^3
ρ_0	=	atmospheric reference density, kg/m^3
σ	=	standard deviation
ς	=	ablation coefficient, s^2/m^2
τ_{lum}	=	luminous efficiency
Φ	=	state transition matrix
ω	=	Earth's angular velocity vector, rad/s

Subscripts

c	=	camera frame
D	=	drag
H	=	heat transfer

Presented as Paper 2012-1298 at the 50th AIAA Aerospace Sciences Meeting including the New Horizons Forum and Aerospace Exposition, Nashville, Tennessee, 9–12 January 2012; received 15 February 2012; revision received 20 July 2012; accepted for publication 23 July 2012; published online 1 March 2013.

*Doctoral Candidate, Department of Aeronautics and Astronautics, West Zone Building 4, 744 Motooka Nishi-ku. Senior Member AIAA.
†Consultant, 5808 Bell Creek Road. Senior Member AIAA.
‡Assistant Research Professor, Institute of Astronomy, 300 Jhongda Road.
§Chief of Research, Space Exploration Centre, 3-1-1 Yoshinodai.

i = inertial frame
k = discrete time instant
L = lift
t = trajectory frame

Superscripts

$-$ = filter a priori value
$+$ = filter updated value
$*$ = reference value

Accents

$\bar{}$ = batch a priori value
$\hat{}$ = estimated value

I. Introduction

THE Hayabusa technology demonstration mission of the Japan Aerospace Exploration Agency (JAXA) ended successfully on 13 June 2010 with the planned atmospheric reentry of the asteroid sample return capsule and main spacecraft. These bodies reentered the atmosphere at night over the Woomera Prohibited Area (WPA) in South Australia, creating bright fireballs. As part of the capsule recovery efforts, JAXA [1] and NASA [2] organized several observation systems to observe the reentry and provide data on the capsule and reentering spacecraft. One of these systems was used to estimate the capsule's trajectory using an extended Kalman filter (EKF) and ground-based camera measurements [3]. The present paper focuses on the postflight trajectory estimation of the main spacecraft, rather than the capsule, using a modified version of the estimation system described in [3]. The objective of the present work is to characterize the breakup of the main Hayabusa spacecraft, which also has implications for general studies of the atmospheric reentry of spacecraft.

Modeling of spacecraft disintegration during reentry has been an active area of research for many years, which has often come to the attention of the aerospace community following high-profile reentry events. One goal of such research is to use fundamental aerothermodynamic principles to predict the heating and breakup of reentering spacecraft, used to assess the risk [4] of surviving fragments impacting the ground. Several computational tools exist to predict the reentry heating and disintegration of spacecraft. NASA's Object Reentry Survival Analysis Tool (ORSAT) tool has been used to predict the reentry survivability hazard of several spacecraft and rocket bodies [5–8]. The vehicle breakup analysis tool is a Jet Propulsion Laboratory/Raytheon package; Salama et al. [9] describe its use for analyzing the off-nominal Earth return of the Genesis spacecraft. The European Space Agency (ESA) uses the Spacecraft Atmospheric Reentry and Aerothermal Breakup code [10–12]. Reference [13] shows another example of a numerical simulation software. Others have used a probabilistic modeling approach to account for the inherent uncertainty in reentry modeling parameters [14,15].

JAXA generated its own predictions of the Hayabusa spacecraft's disintegration and reentry hazard to obtain permission from the Australian government for recovery operations at WPA. Although the details of these codes and simulation results have not been widely published by JAXA, some general predictions have been shared and are discussed in Sec. V. A program called Range Safety Template Toolkit was used by an Australian team as an independent verification of the Hayabusa sample return capsule's risk of reentry failure [16,17], but it does not appear to have been applied to the main spacecraft.

It has been claimed [18] that there is a need to collect more flight data on destructive reentry. Such data may be useful to further validate these and other reentry modeling methods. However, data on destructive reentry (i.e., flight telemetry, optical measurements, recovered fragments) are scarce; the precise locations of unplanned reentry events (e.g., orbital decay of space debris) are difficult to predict, and planned reentry events (e.g., disposal) are usually performed over isolated areas. Both cases make it difficult to position appropriate sensors or recover pieces. Recently a "black box" flight data recorder was proposed as one method to overcome some of these difficulties in collecting reentry data [19,20]. Although not using flight data, some studies [21,22] have compared the results from different reentry codes as one means of cross validation.

There are several examples in the literature of collecting data from reentry observations. NASA's ORSAT reentry simulation code was validated during its development [5] using flight-test data collected by NASA and Sandia Corporation in the 1960s from inert models of nuclear fuel rods [23]; data were collected during these tests using telemetered test vehicles and ground-based and airborne optical instruments [24]. The citations in [2] provide additional historical examples from the 1960s and 1970s. ORSAT was used to model the Space Shuttle *Columbia* for the postflight accident investigation; the heating evidence on some recovered fragments showed discrepancies with the tool's predictions [25]. Video captured of the *Columbia* destruction was used to identify separation time and ballistic coefficients of several fragments of the vehicle [26]. Airborne cameras also recorded the first reentry of ESA's Automated Transfer Vehicle [27]; de Pasquale et al. [28] report that the estimated trajectories of major fragments were close to predicted, but they omit details of the estimation method. Optical observations of the Genesis [29] and Stardust [30] sample return capsules provided data on radiation spectra and other data useful for evaluating the thermal protection systems.

This paper makes the following contributions. Mission results are presented on the trajectory estimation of the breakup of the main Hayabusa spacecraft. Others have done simulations of low-Earth-orbit (LEO) debris reentry estimation in the past [31,32]. This paper expands on the EKF for reentry estimation given in [31] by adding the batch initialization process, and by using the unit vector as the measurement instead of the angles. This paper also makes contributions to the area of space debris reentry and survivability, because the drag and lift ballistic coefficients for the disintegrating spacecraft fragments are estimated. This study is unique because 80 individual reentry fragments are analyzed, as opposed to [33], which estimated the trajectories of a smaller number of bright Hayabusa fragments (or fragment groups) using meteor-based methods and multiple cameras. Watanabe et al. [34] analyzed the number of Hayabusa fragments over time using similar video as in the present study, but did not attempt to estimate the trajectories. The Hayabusa reentry mission itself offers a unique opportunity because it is one of the few times such measurements have been made on a disintegrating spacecraft reentering at superorbital velocity.

Furthermore, the ablation coefficients of several Hayabusa fragments are estimated using methods borrowed from meteor researchers. Meteor physics have been used since the 1960s by aerodynamicists and engineers to provide insight into atmospheric entry [35–39]. The ablation coefficient is often used to characterize the material composition and ablation processes of meteors. Here, it is also used to check the validity of the estimated drag ballistic parameters and to compare results with other estimation methods used on Hayabusa reentry observations [33]. Note, however, that the trajectory estimation methods used in this paper and those typically used by meteor researchers (e.g., [40–42]) are fundamentally different: the three-dimensional trajectory estimation of a meteor requires multistation line-of-sight (LOS) measurements because there is no a priori knowledge (e.g., the plane of the reference trajectory) that can be used to form an initial state estimate. In this paper, the ablation coefficient is calculated without explicitly including the mass-loss equation in the trajectory estimation procedure (i.e., the ablation coefficient is calculated after the trajectory is estimated, in contrast with meteor methods in which the mass-loss equation is included directly in the method of solution).

This paper is organized as follows. First, the observation system design and calibration are discussed. Then a description is given of the trajectory dynamics model used in the estimation system, as well as the design and configuration of the estimation algorithm itself. Next, the results of the trajectory estimation are given for all objects, followed by the analysis of the estimated ablation coefficients. Although this paper does not focus on the capsule's trajectory

Table 1 Camera and lens specifications (GOS3N)

Item	Specification
CCD type	WATEC WAT-100N
Total pixels	811 × 508
Effective pixels	768 × 494
Gamma setting	Off
Focal length	25 mm
Focal ratio	1.2
Field of view	14.59 × 10.97 deg

estimation, the drag and lift ballistic coefficients of the capsule are estimated as one means of validating the estimation system.

II. Observation System

Of the four ground observations sites (GOS) established by JAXA near the reentry area [1], the camera used in this study was located at GOS3. The GOS locations were chosen based on their geometric diversity and for logistical reasons (see [3] for location details). The commercial off-the-shelf charge-coupled device (CCD) video camera, with specifications given in Table 1, was used at GOS3. A collection of several videos of the reentry (including video recorded from GOS3) can be found online at JAXA's digital archives.[¶]

In contrast with the stationary, wide-field-of-view (FOV) cameras used for rapid trajectory estimation of the capsule [3], the single camera used in this study had a narrow FOV and was manually tracked to follow the capsule. Although the original intent of this video system was to collect video of the capsule, the video also contained data on the main spacecraft and fragments, making it useful for the present study. Figure 1 shows an image sequence of the reentry captured with this narrow-FOV observation system, where the times are measured in Coordinated Universal Time (UTC) (with the reentry epoch at 200 km altitude defined as 13 June 2010 13:51:12.19). A commercial-grade GPS receiver was used with custom-written software to record the GPS time signal onto each video frame of the wide-FOV cameras. The narrow-FOV camera times were estimated by comparing its recorded flare brightness (Fig. 2) with the time-stamped wide-FOV video, resulting in a 1σ timing uncertainty of 0.01 s.

Figure 2 shows an approximate measure of the main spacecraft's brightness, as observed by several cameras (where "L" or "R" following the GOS number indicates the left or right wide-FOV cameras described in [3], and GOS3N indicates the narrow-FOV camera described in Table 1). The approximate brightness in Fig. 2 is calculated as the number of pixels in the fireball exceeding a certain threshold, normalized by the maximum fireball pixel count observed by a given camera. Although this brightness is not calibrated for absolute magnitude studies, it is useful for describing the relative change in brightness during the destructive reentry. Based on the spacecraft flare brightness and the time when the fragments become visible, the spacecraft main disintegration can be described as beginning during the first large flare event around 13:52:13 and ending during the second large flare event at 13:52:20.

See [3] for a description of the procedure for calibrating the camera lens model and estimating the camera frame $\mathcal{F}_c$ attitude relative to the inertial frame. To summarize the procedure: The background stars in each video frame were manually identified and measured in pixel coordinates; these star measurements were used in an iterative procedure to estimate simultaneously the camera model (i.e., description of lens distortion, etc.) and camera frame attitude. Comparing the cataloged star positions with their measured directions from the calibrated camera model results in errors having a mean of approximately zero and a variance of 1×10^{-4} rad.

After performing this calibration, the pixel coordinates of a reentry object were measured in each video frame and used with the camera model and attitude to construct $\hat{\rho}$, the unit line-of-sight vector in $\mathcal{F}_i$. Although the catalog star positions used for the camera calibration account for astronomical refraction, the measured $\hat{\rho}$ require a separate correction for the refraction experienced by targets within the atmosphere. The video was manually analyzed frame by frame to identify reentry objects and to correlate a given object's measurements between frames. Only reentry objects that were clearly defined on multiple frames and that were less likely to be misidentified (e.g., by passing behind another target or reentry wake) were kept for analysis.

[¶]Data available online at http://jda.jaxa.jp/en/ [retrieved 17 July 2012].

III. Trajectory Dynamics

A three-degree-of-freedom, point-mass model is used to describe the translational motion of a reentering body:

$$\ddot{\mathbf{r}} = -\frac{\mu}{r^3}\mathbf{r} + \mathbf{a}_L + \mathbf{a}_D \tag{1}$$

in which the two-body gravity, lift, and drag accelerations are considered. Figure 3 shows these accelerations acting on the body and introduces several reference frame definitions. Frame $\mathcal{F}_i$ is the inertial frame centered on the Earth, here taken to be the J2000

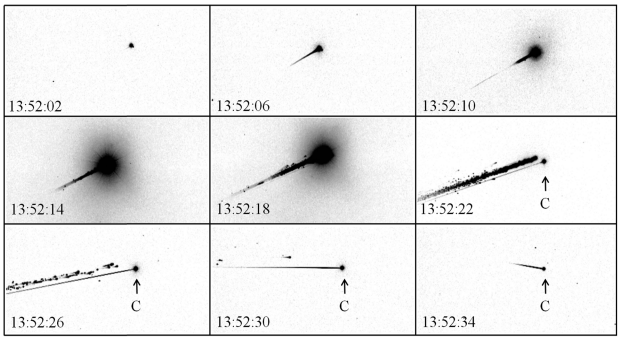

Fig. 1 Inverted grayscale image sequence of reentry, showing capsule (marked with "C") and spacecraft fragments, with UTC time rounded to nearest second.

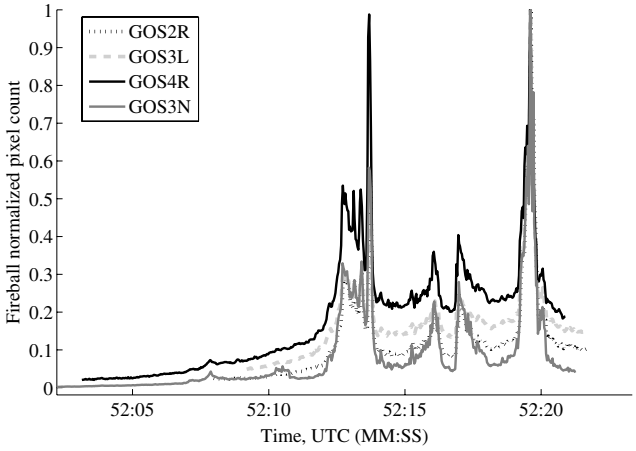

Fig. 2 Normalized pixel count in main spacecraft fireball.

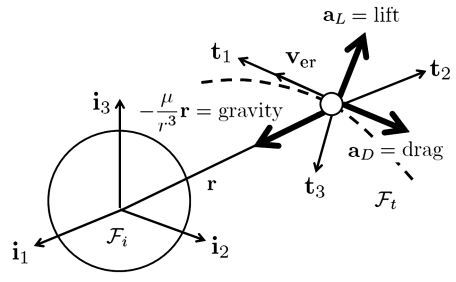

Fig. 3 Sketch of reentry dynamics and reference frames.

reference frame. Frame $\mathcal{F}_t$ is centered on the body, with the one-axis unit vector aligned with the body's Earth-relative velocity vector $\mathbf{v}_{\text{er}}$, the two-axis unit vector in the cross-track direction, and the three-axis unit vector completing the right-handed coordinate system. The unit vectors along these three $\mathcal{F}_t$ axes, expressed in $\mathcal{F}_i$, are

$$\mathbf{t}_{1i} = \frac{\mathbf{v}_{\text{er}}}{|\mathbf{v}_{\text{er}}|} \tag{2}$$

$$\mathbf{t}_{2i} = \frac{\mathbf{t}_{1i} \times \mathbf{r}}{|\mathbf{t}_{1i} \times \mathbf{r}|} \tag{3}$$

$$\mathbf{t}_{3i} = \mathbf{t}_{1i} \times \mathbf{t}_{2i} \tag{4}$$

The Earth-relative velocity expressed in $\mathcal{F}_i$ is

$$\mathbf{v}_{\text{er}} = \mathbf{v} - \omega \times \mathbf{r} \tag{5}$$

The lift and drag ballistic coefficients are defined, respectively, as $\beta_L \equiv SC_L/m$ and $\beta_D \equiv SC_D/m$, and the lift and drag accelerations can be easily expressed in $\mathcal{F}_t$ with

$$\mathbf{a}_{L,t} = [\,0 \quad 0 \quad -\rho v_{\text{er}}^2 \beta_L/2\,]^T \tag{6}$$

$$\mathbf{a}_{D,t} = [\,-\rho v_{\text{er}}^2 \beta_D/2 \quad 0 \quad 0\,]^T \tag{7}$$

These accelerations are expressed in $\mathcal{F}_i$ using the rotation matrix $\mathbf{C}^{it}$, that is, $\mathbf{a}_L = \mathbf{C}^{it}\mathbf{a}_{L,t}$ and $\mathbf{a}_D = \mathbf{C}^{it}\mathbf{a}_{D,t}$, where $\mathbf{C}^{it} = [\,\mathbf{t}_{1i} \quad \mathbf{t}_{2i} \quad \mathbf{t}_{3i}\,]$. Thus, this dynamics model only considers the forces acting in the instantaneous trajectory plane consisting of the Earth-relative velocity vector and position vector. Also, the aerodynamics model neglects the effects of atmospheric winds relative to the surface of the Earth.

The atmospheric density is modeled with the CIRA72 exponential model:

$$\rho = \rho_0 \exp\left[-\frac{h_{\text{ellp}} - h_0}{H}\right] \tag{8}$$

where ρ_0, h_0, and H are defined over 10 km altitude bands, resulting in a piecewise-continuous density variation (see [43], pp. 537 for a table of these parameters). The term h_{ellp} is the altitude above an ellipsoidal Earth:

$$h_{\text{ellp}} = r - R_e\left[1 + \frac{r_3^2}{r^2}\left(\frac{R_e^2}{R_p^2} - 1\right)\right]^{-\frac{1}{2}} \tag{9}$$

where $\mathbf{r} = [\,r_1 \quad r_2 \quad r_3\,]^{\text{T}}$.

IV. State Estimation

Because the detailed fragmentation of the Hayabusa spacecraft was only captured on one of the JAXA team's cameras, it is impossible to do a three-dimensional trajectory reconstruction using geometric methods (e.g., triangulation). The EKF can be used with angles-only measurements from the single ground site to estimate the trajectory, assuming an initial state estimate and a model of the state dynamics are available. This study makes use of the following assumption: Because the nominal capsule trajectory is known a priori, and the capsule's estimated reentry trajectory was shown to match closely with the nominal trajectory [3], the fragments are assumed to be in the same plane as the capsule's nominal trajectory to calculate an initial state estimate. A similar planar restriction was used in [26] to estimate the relative motion of debris fragments with respect to the *Columbia* orbiter's reference trajectory using single-station video data. Although the line-of-sight measurements from a single ground site used in the present study cannot provide range information, they allow trajectory estimates that are valid within the assumed dynamics model.

This section describes several processes that make up the state estimation system: the EKF, the batch initialization, the method for generating an initial state estimate, and the configuration used for the present study. Although the EKF is a sequential estimation method, in this study there was no requirement to process data in real time and thus all processing was done after the reentry had occurred.

A. Extended Kalman Filter

The continuous-discrete form of the EKF [44] is used for this study, where the state vector is defined as $\mathbf{X} \equiv [\,\mathbf{r}^T \quad \mathbf{v}^T \quad \beta_D \quad \beta_L\,]^{\text{T}}$. The discrete-time measurement vector at time $t_k : k \in \{1, \ldots, K\}$ is

$$\mathbf{Y}_k = \mathbf{G}(\mathbf{X}_k) + \epsilon_k \tag{10}$$

where

$$\mathbf{G}(\mathbf{X}_k) = \rho/|\rho| = \hat{\rho} \tag{11}$$

is the 3×1 unit line-of-sight vector, $\rho = \mathbf{r} - \mathbf{c}$, and ϵ_k is the measurement noise modeled as a zero-mean, Gaussian white-noise random process with covariance $\mathbf{R}_k = E(\epsilon_k \epsilon_k^{\text{T}})$.

The nonlinear system of state equations is written in continuous-time form as

$$\dot{\mathbf{X}}(t) = \mathbf{F}(\mathbf{X}, t) + \mathbf{q}(t) \tag{12}$$

where $\mathbf{q}(t)$ is the process noise, modeled as a zero-mean, Gaussian white-noise random process with autocorrelation function $\mathbf{Q}(t)$, such that $E[\mathbf{q}(t)\mathbf{q}^{\text{T}}(\tau)] = \mathbf{Q}(t)\delta(t - \tau)$. The dynamics of β_D and β_L are modeled as an integral of zero-mean, Gaussian white noise (i.e., random walk). Thus, the system dynamics from Eq. (12) are written as

$$\dot{\mathbf{X}}(t) = \begin{bmatrix} \mathbf{v} \\ \ddot{\mathbf{r}} \\ \mathbf{0}_{2\times 1} \end{bmatrix} + \begin{bmatrix} \mathbf{q}_{\mathbf{r}} \\ \mathbf{q}_{\mathbf{v}} \\ \mathbf{q}_{\beta} \end{bmatrix} \tag{13}$$

The state estimate $\hat{\mathbf{X}}(t) = E(\mathbf{X}(t))$ has a state estimate error covariance of

$$\mathbf{P}(t) = E\{[\mathbf{X}(t) - \hat{\mathbf{X}}(t)][\mathbf{X}(t) - \hat{\mathbf{X}}(t)]^{\text{T}}\} \tag{14}$$

The Jacobian of the state equations is

$$\mathbf{A}(\hat{\mathbf{X}}, t) = \left[\frac{\partial \mathbf{F}}{\partial \mathbf{X}}\right]_{\hat{\mathbf{X}}(t)} \tag{15}$$

where the subscript denotes evaluation on $\hat{\mathbf{X}}(t)$. Likewise, the Jacobian of the measurement equation is

$$\mathbf{H}_k(\hat{\mathbf{X}}_k^-) = \left[\frac{\partial \mathbf{G}(\mathbf{X})}{\partial \mathbf{X}}\right]_{\hat{\mathbf{X}}_k^-} \tag{16}$$

The state estimate is propagated by numerically integrating the nonlinear differential equations of motion from t_{k-1} to t_k:

$$\hat{\mathbf{X}}_k^- = \hat{\mathbf{X}}_{k-1}^+ + \int_{t_{k-1}}^{t_k} \mathbf{F}(\hat{\mathbf{X}}, \tau)\, \mathrm{d}t \tag{17}$$

and the continuous-time Lyapunov differential equation for the state estimate error covariance

$$\dot{P}(t) = \mathbf{A}(\hat{\mathbf{X}}, t)\mathbf{P}(t) + \mathbf{P}(t)\mathbf{A}^{\text{T}}(\hat{\mathbf{X}}, t) + \mathbf{Q}(t) \tag{18}$$

is propagated over the same time interval:

$$\mathbf{P}_k^- = \mathbf{P}_{k-1}^+ + \int_{t_{k-1}}^{t_k} \dot{\mathbf{P}}(\tau)\,\mathrm{d}t \tag{19}$$

The integrals in Eqs. (17) and (19) are solved numerically using a fourth-order Runge–Kutta method. The Kalman gain matrix $\mathbf{K}_k$ is defined as

$$\mathbf{K}_k = \mathbf{P}_k^- \mathbf{H}_k^T(\hat{\mathbf{X}}_k^-)[\mathbf{H}_k(\hat{\mathbf{X}}_k^-)\mathbf{P}_k^- \mathbf{H}_k^T(\hat{\mathbf{X}}_k^-) + \mathbf{R}_k]^{-1} \tag{20}$$

The state estimate is updated at time t_k with the help of the measurements $\mathbf{Y}_k$ with

$$\hat{\mathbf{X}}_k^+ = \hat{\mathbf{X}}_k^- + \mathbf{K}_k[\mathbf{Y}_k - \mathbf{G}(\hat{\mathbf{X}}_k^-)] \tag{21}$$

where $\mathbf{y}_k \equiv \mathbf{Y}_k - \mathbf{G}(\hat{\mathbf{X}}_k^-)$ is the EKF measurement residual. The state estimate error covariance is updated with

$$\mathbf{P}_k^+ = [\mathbf{I} - \mathbf{K}_k \mathbf{H}_k(\hat{\mathbf{X}}_k^-)]\mathbf{P}_k^- \tag{22}$$

This estimator includes the aerodynamic parameters β_L and β_D in the state vector, whereas the EKF state vector in [3] includes a density scale factor for estimating the capsule's trajectory. The reason for this difference is that the aerodynamic parameters of the capsule were assumed known a priori, whereas they are assumed unknown for the main spacecraft fragments. There are also differences between the current EKF and that in [31]: No post-EKF smoother is used here; β_D is used directly in the state, rather than its square root; the measurements are the unit LOS vector, rather than the topocentric right ascension and declination angles; and a batch initialization process is added. The first two differences are made for the sake of simplicity in the formulation, and the third was added to avoid kinematic singularities near the celestial poles. The batch initialization is used to refine the initial state estimate $\hat{\mathbf{X}}_0$ and initial state estimate covariance matrix $\mathbf{P}_0$, which are both required inputs to the EKF.

B. Batch Initialization

One advantage of using this batch initialization technique (compared with simply defining a diagonal matrix) is that the resulting $\mathbf{P}_0$ contains off-diagonal terms that capture the dynamic coupling between states. Similar batch initialization processes have been used for missile tracking studies during their exoatmospheric [45] and boost [46] phases to improve estimation performance. The formulation in this subsection is based on a batch orbit determination algorithm in [47].

The state deviation vector is defined as $\mathbf{x}(t) \equiv \mathbf{X}(t) - \mathbf{X}^*(t)$, where $\mathbf{X}^*$ is the reference trajectory. A given iteration of the batch process has initial conditions $\mathbf{X}^*(t_0)$, an a priori state deviation vector estimate $\bar{\mathbf{x}}_0$, and an a priori state error covariance estimate $\bar{\mathbf{P}}_0$. An iteration of the batch process results in a new estimate of the covariance $\mathbf{P}_0$ and the state deviation vector $\hat{\mathbf{x}}_0$, both at t_0. The so-called normal equation for a given iteration of the batch processor is

$$(\mathbf{H}^T\mathbf{R}^{-1}\mathbf{H} + \bar{P}_0^{-1})\hat{\mathbf{x}}_0 = \mathbf{H}^T\mathbf{R}^{-1}\mathbf{y} + \bar{\mathbf{P}}_0^{-1}\bar{\mathbf{x}}_0 \tag{23}$$

Note that the terms $\mathbf{R}$, $\mathbf{H}$, and $\mathbf{y}$ without the subscript k denote the matrix quantities for the entire batch. Because the observations are assumed to be uncorrelated in time (i.e., $\mathbf{R}$ is a block diagonal matrix), the following summations are used to populate the batch matrix quantities:

$$\mathbf{H}^T\mathbf{R}^{-1}\mathbf{H} = \sum_{k=1}^{L} [\mathbf{H}_k \Phi(t_k, t_0)]^T \mathbf{R}_k^{-1} \mathbf{H}_k \Phi(t_k, t_0) \tag{24}$$

$$\mathbf{H}^T\mathbf{R}^{-1}\mathbf{y} = \sum_{k=1}^{L} [\mathbf{H}_k \Phi(t_k, t_0)]^T \mathbf{R}_k^{-1} \mathbf{y}_k \tag{25}$$

Analogous to the measurement residual in the EKF, the term $\mathbf{y}_k$ in Eq. (25) is evaluated with $\mathbf{y}_k = \mathbf{Y}_k - \mathbf{G}(\mathbf{X}_k^*)$.

The reference trajectory $\dot{\mathbf{X}}^* = \mathbf{F}(\mathbf{X}^*, t)$ with initial conditions $\mathbf{X}^*(t_0)$, and state transition matrix $\dot{\Phi}(t, t_0) = \mathbf{A}(\mathbf{X}^*, t)\Phi(t, t_0)$ with initial conditions $\Phi(t_0, t_0) = \mathbf{I}$, are solved via the same Runge–Kutta numerical integration mentioned earlier. Note that the batch filter formulation does not include process noise, that is, the system dynamics in $\mathbf{F}(\mathbf{X}^*, t)$ include only the first term on the right-hand side of Eq. (13). The estimated initial covariance and state deviation vector are found from a given iteration of the batch process with

$$\mathbf{P}_0 = (\mathbf{H}^T\mathbf{R}^{-1}\mathbf{H})^{-1} \tag{26}$$

$$\hat{\mathbf{x}}_0 = \mathbf{P}_0\mathbf{H}^T\mathbf{R}^{-1}\mathbf{y} \tag{27}$$

The batch process is iterated a specified number of times with the following changes to the inputs: $\hat{\mathbf{x}}_0$ is added to $\mathbf{X}_0^*$; $-\hat{\mathbf{x}}_0$ is added to $\bar{\mathbf{x}}_0$; and the original value of $\bar{\mathbf{P}}_0$ is reused each time. If the batch process has completed its iterations, the initial state estimate $\hat{\mathbf{X}}_0 = \mathbf{X}_0^* + \hat{\mathbf{x}}_0$ and covariance matrix from Eq. (26) are fed into the EKF.

C. Initial State Estimate

An initial state estimate is needed for the batch initialization process. For an exoatmospheric orbiting body, there are several methods available for obtaining an initial orbit estimate using angles-only measurements (e.g., [43], chapter 7). For the present problem, the reentry fragments are already experiencing drag, and so it is assumed that they are approximately coplanar with the nominal capsule trajectory and that their reentry path can be approximated with a straight line with constant speed during a short measurement span. Note that the ballistic coefficient initial guesses are defined separately in the next section.

If it is assumed that the reentry body is in the plane of the capsule's nominal trajectory, then this information can be used to approximate the range from the sensor to the body and thus construct an approximate position vector. Let $\hat{\mathbf{n}}$ be the unit vector normal to the nominal reentry plane. Then the planar constraint on $\mathbf{r}$ yields

$$\hat{\mathbf{n}} \cdot \mathbf{r} = \hat{\mathbf{n}} \cdot (\mathbf{c} + \rho) = 0 \tag{28}$$

Because $\rho = \hat{\rho}|\rho|$, this can be rearranged to solve for $|\rho|$:

$$|\rho| = -(\hat{\mathbf{n}} \cdot \mathbf{c})/(\hat{\mathbf{n}} \cdot \rho) \tag{29}$$

and thus the position vector is $\mathbf{r} = \mathbf{c} + \hat{\rho}|\rho|$.

Given the approximated position vector "measurements" $\mathbf{r}$, a linear least-squares approach is used to estimate $\mathbf{v}_0$. This procedure is equivalent to the polynomial batch filter initialization from [46], in which the acceleration and jerk terms have been neglected. The position vectors can then be written as $\mathbf{r}_k = \mathbf{v}_0(t_k - t_0) + \mathbf{r}_0$, and then rearranged as $\Delta\mathbf{r}_k \equiv \mathbf{r}_k - \mathbf{r}_0 = \Delta t_k \mathbf{v}_0$. Defining the matrices

$$\mathcal{Y} \equiv \begin{bmatrix} \Delta\mathbf{r}_1 \\ \vdots \\ \Delta\mathbf{r}_J \end{bmatrix} \tag{30}$$

$$\mathcal{C} \equiv \begin{bmatrix} \Delta t_1 I_{3\times3} \\ \vdots \\ \Delta t_J I_{3\times3} \end{bmatrix} \tag{31}$$

then $\mathcal{Y} = \mathcal{C}\mathbf{v}_0$, which can be solved with

$$\mathbf{v}_0 = (\mathcal{C}^T\mathcal{C})^{-1}\mathcal{C}^T\mathcal{Y} \tag{32}$$

D. Estimator Configuration

For the batch initialization, the initial covariance is set to

$$\bar{\mathbf{P}}_0 = \mathrm{diag}(\sigma^2_{\mathrm{pos}}, \sigma^2_{\mathrm{pos}}, \sigma^2_{\mathrm{pos}}, \sigma^2_{\mathrm{vel}}, \sigma^2_{\mathrm{vel}}, \sigma^2_{\mathrm{vel}}, \sigma^2_{\beta_D}, \sigma^2_{\beta_L}) \tag{33}$$

where $\sigma^2_{\mathrm{pos}} = 1 \times 10^4$ m^2, $\sigma^2_{\mathrm{vel}} = 1 \times 10^4$ m^2/s^2, $\sigma^2_{\beta_D} = 1 \times 10^{-2}$ m^4/kg^2, and $\sigma^2_{\beta_L} = 1 \times 10^{-4}$ m^4/kg^2. The initial guesses of β_D and β_L used for each reentry target are 5.3×10^{-3} m^2/kg and 0 m^2/kg, respectively. Regarding the number of points, the choice of L affects the suitability of $\mathbf{P}_0$: Setting L too low may not capture the correlations between the position and velocity, whereas setting L too high will also result in smaller error correlations [45]. Also, although the EKF models the dynamic ballistic coefficients via process noise terms, the batch filter includes no process noise and thus assumes constant ballistic coefficients. Thus, the batch filter may diverge if L is too high and a given reentry object has significantly dynamic β_D or β_L. It was found in this application that running the batch for 10 iterations, with $L = 100$ points per iteration, produced acceptable inputs to the EKF. For some fragments with short measurement spans, L was set to the total number of measurements (the minimum of which was $L = 30$). Furthermore, $J = 9$ measurements were used to find the initial state estimate for each object.

The EKF's process noise $\mathbf{Q}(t)$ is defined through trial and error as part of the estimator design process. Tardy and Kluever [32] use a "dynamic integral state" model for the process noise, in which the estimated velocity and ballistic coefficients are included in $\mathbf{Q}(t)$. This study uses the simpler model from [31], in which $\mathbf{Q}(t)$ is assumed to be a constant diagonal matrix, with the position and velocity terms set to zero, leaving only terms for β_D and β_L:

$$\mathbf{Q}(t) = \mathbf{Q} = \mathrm{diag}(0, 0, 0, 0, 0, 0, 1 \times 10^{-8}\ \mathrm{m^4\,kg^{-2}\,s^{-1}}, 1 \times 10^{-8}\ \mathrm{m^4\,kg^{-2}\,s^{-1}}) \tag{34}$$

The definition of $\mathbf{R}_k$ assumes only zero-mean Gaussian noise in the image plane having variance σ_{meas}. Other sources of error in the measurements (e.g., ground site position knowledge) are assumed to be much smaller and are thus neglected. Shuster [48] showed that, for a unit line-of-sight measurement from a narrow-FOV camera, $\mathbf{R}_k$ expressed in $\mathcal{F}_c$ can be approximated with $\sigma^2_{\mathrm{meas}}\mathbf{I}_{3\times3}$ (and this diagonal matrix $\mathbf{R}_k$ is the same when expressed in $\mathcal{F}_c$ or $\mathcal{F}_i$). For the debris fragments, a variance of $\sigma_{\mathrm{meas}} = 4 \times 10^{-4}$ rad is selected. A value of $\sigma_{\mathrm{meas}} = 1 \times 10^{-3}$ rad is used for the main spacecraft to account for the increased brightness and the corresponding CCD saturation.

V. Trajectory Estimation Results

A total of 230 fragments were first tracked in the video. Because some fragments had short measurement spans, it was decided to only analyze fragments having at least 1 s of data (i.e., around 30 measurements). Of the approximately 100 fragments that met this minimum number of measurements, approximately 20 had poor estimation results; the estimator either diverged or produced unrealistic values (e.g., negative drag). These 20 fragments may have been poorly measured during the video-analysis step, or the estimator configuration may have been insufficient for these objects. The rest of the analysis is restricted to the remaining 80 fragments that had acceptable results.

Table 2 shows some quantities that evaluate the performance of the estimator for the 80 fragments. The first four quantities represent the state elements in $\hat{\mathbf{x}}_0$ after the first batch iteration, which give an indication of how much correction is needed to the initial state guess $\mathbf{X}^*_0$. These values of $\hat{\mathbf{x}}_0$ are reasonable considering the initial covariance $\mathbf{P}_0$ defined in Eq. (33) and the approximations used in forming the initial state estimate (Sec. IV.C). Also, the rms of the observation residuals from both the batch process and the EKF are used as a measure of their effectiveness. The rms for the EKF is

Table 2 Summary of fragment estimation results

Quantity	Mean	Standard deviation
Norm of $\mathbf{r}$ elements of $\hat{\mathbf{x}}_0$, km	0.07	0.03
Norm of $\mathbf{v}$ elements of $\hat{\mathbf{x}}_0$, km/s	0.13	0.08
β_D element of $\hat{\mathbf{x}}_0$, m^2/kg	0.07	0.07
β_L element of $\hat{\mathbf{x}}_0$, m^2/kg	-5×10^{-4}	4×10^{-3}
Batch rms, rad	2×10^{-4}	7×10^{-5}
EKF rms, rad	2×10^{-4}	7×10^{-5}

$$\mathrm{rms} = \left(\frac{1}{M}\sum_{k=1}^{K}\mathbf{y}_k^T\mathbf{y}_k\right)^{1/2} \tag{35}$$

where $M = K \times 3$ is the total number of measurements for a given reentry fragment (and similarly for the batch process, where L replaces K). The mean and standard deviation of these rms values for all 80 fragments are given in Table 2 as a summary of the results (where the batch rms values are for the final iteration only). Thus, the measurement residual rms for both the batch and EKF are around 2×10^{-4} rad, which is half of the assumed measurement noise variance of $\sigma_{\mathrm{meas}} = 4 \times 10^{-4}$ rad. The time history of these residuals do not show significant biases; Fig. 4 gives an example of the EKF measurement residuals for one of the fragments. Figure 5 is a plot of the EKF measurement residuals for the main spacecraft fireball, which shows some biases likely due to the higher CCD saturation and difficulty in accurately measuring the fireball centroid (recall Fig. 1).

Figures 6–8 show the EKF's estimated $r = |\mathbf{r}|$, $v = |\mathbf{v}|$, and β_D, where the error bars represent the 1-σ variances (i.e., the square root of the trace of the corresponding elements in $\mathbf{P}^+_k$). The data gap from 13:52:19 to 13:52:22 corresponds to a large flare event (see Fig. 2), which prevented accurate fragment measurements. Comparing the main spacecraft's estimated v in Fig. 7 with the preflight prediction of approximately 12.1 km/s, it is clear that the EKF's estimate is offset by nearly 0.5 km/s. Although this discrepancy is within the 3-σ estimation uncertainties, it may be attributable to the filter's poor observability of the velocity at the beginning of the reentry with a nearly head-on view.

The altitude range of the main disintegration event (from 13:52:13 to 13:52:20 in Fig. 2) can be estimated by propagating the main spacecraft's path forward in time in Fig. 6; these times correspond to radial positions between 6440 and 6430 km (i.e., approximately 70–56 km altitude). Separate spectroscopic observations [49] support this conclusion; lithium from the Li-ion battery was detected at 55 km altitude, and xenon from the remaining ion engine propellant was detected from 63 to 55 km altitude. The observed result is slightly

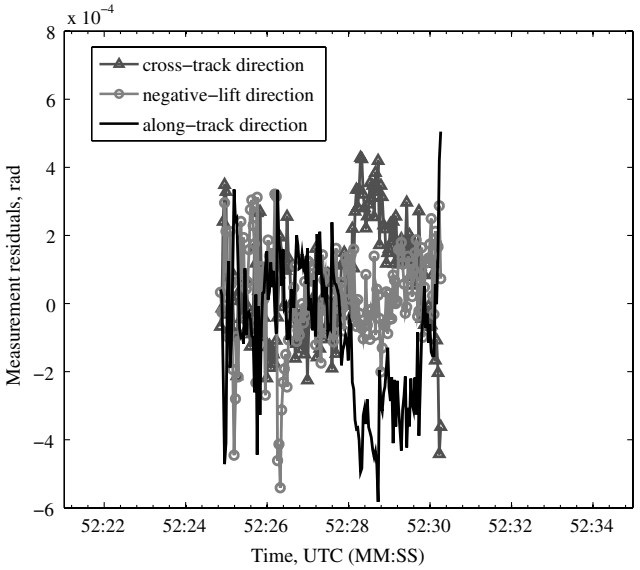

Fig. 4 Example of one fragment's EKF measurement residuals $\mathbf{y}_k$, expressed in $\mathcal{F}_t$.

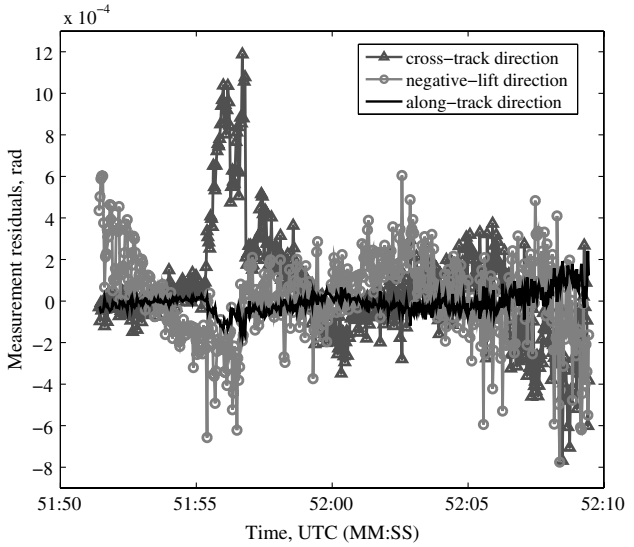

Fig. 5 Main spacecraft's EKF measurement residuals y_k, expressed in $\mathcal{F}_t$.

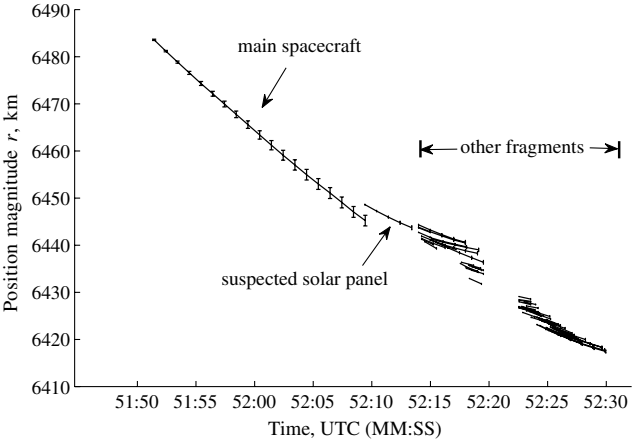

Fig. 6 Estimated radial position from Earth's center (with 1-σ uncertainties).

lower than some LEO debris reentry studies [8,21,50] that cite 70–80 km as the typical altitude of main disintegration.

The first fragment with measurements at 13:52:09 is possibly one of the solar panels. This fragment can be seen in other recorded video [1] around 13:52:07, but was not detectable in this study's camera until 2 s later. According to JAXA's preflight analysis, the solar panels were predicted to separate at 80 km altitude. At 13:52:09, this corresponds to 6448 km (i.e., around 80 km altitude); if indeed this

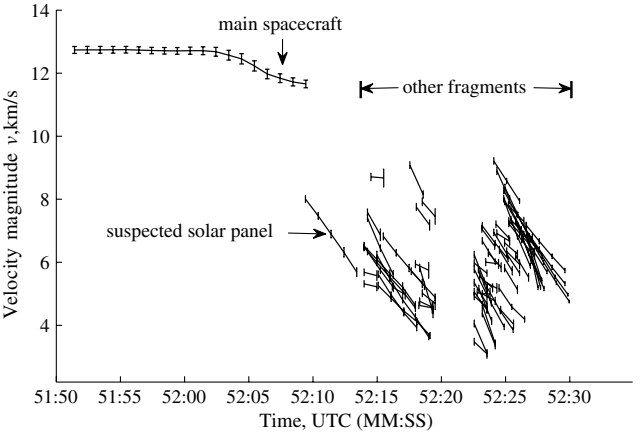

Fig. 7 Estimated inertial velocity (with 1-σ uncertainties).

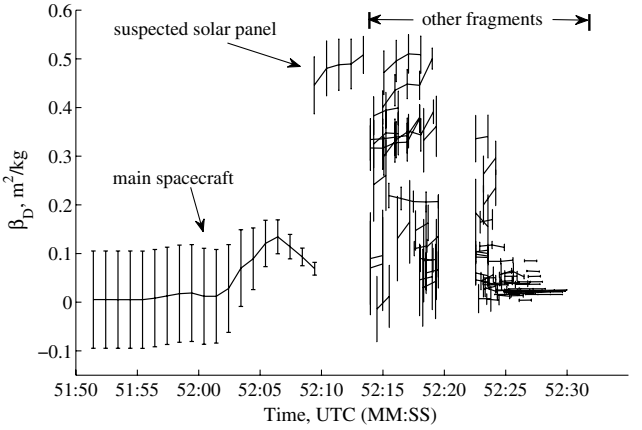

Fig. 8 Estimated drag ballistic coefficient (with 1-σ uncertainties).

first observed fragment is one of the solar panels, this result matches closely with the prediction. This fragment has a high area-to-mass ratio, reflected in the β_D estimate (see Fig. 8), which supports the notion that it is a solar panel. Note that, although a group of fragments appear in Fig. 6 having similar radial position magnitude as the suspected solar panel (i.e., from 13:52:13 to 13:52:19), these fragments have a large angular separation from the solar panel and thus are likely unrelated.

The freestream dynamic pressure ($\rho v_{\text{cr}}^2/2$) can be calculated using an object's estimated position and velocity. Figure 9 shows the freestream dynamic pressure versus geodetic altitude (without error bars); the overall trend of the observed objects as a group is that dynamic pressure increases with decreasing altitude, which is reasonable considering the exponential density increase. However, it is important to note that almost all individual fragments are observed after they have experienced maximum dynamic pressure (i.e., an individual fragment has decreasing dynamic pressure with decreasing altitude). This decreasing dynamic pressure trend (which has also been observed in some meteor fragmentation studies [51]) is likely a feature of the observation system in this case; most fragments are only visible several seconds after a fragmentation event has occurred due to the bright flashes and CCD saturation that tend to accompany these events (Fig. 2).

Figures 10 and 11 show the estimated ballistic coefficients versus dynamic pressure, and Fig. 12 shows the estimated lift-to-drag ratio for the fragments. It is clear that most objects have drag that is one or two orders of magnitude more than the lift. From Figs. 10 and 11, one can see that the drag and lift parameters have less uncertainty at higher dynamic pressure. This result is expected because the

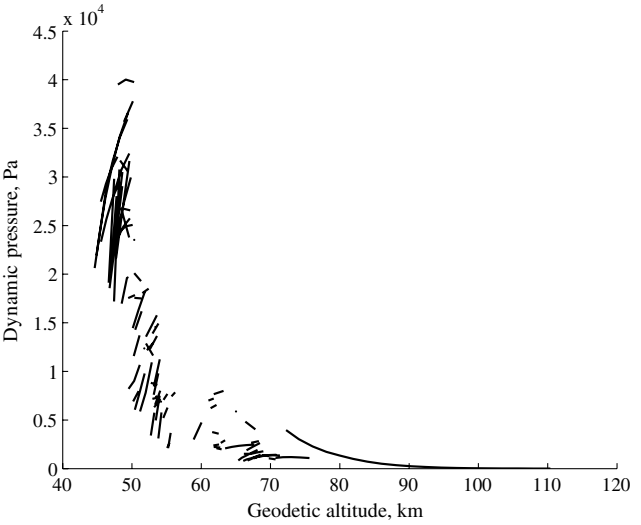

Fig. 9 Dynamic pressure versus altitude of fragments and main spacecraft.

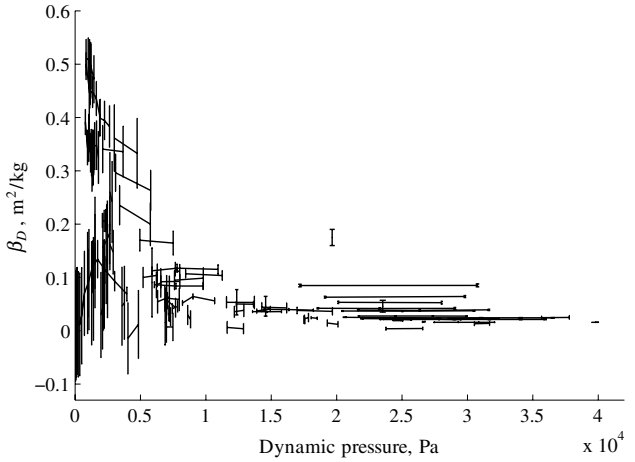

Fig. 10 Estimated drag ballistic coefficient versus freestream dynamic pressure (with 1-σ uncertainties). Uncertainty in the calculated dynamic pressure is ignored in this plot.

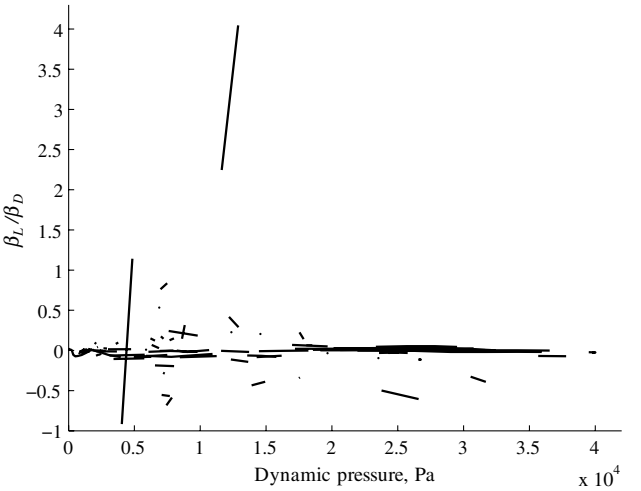

Fig. 12 Lift-to-drag ratio, ignoring uncertainties.

aerodynamic forces are larger at higher dynamic pressure; thus, these states have more effect on the trajectory and are more observable in the estimation process. Also, the fragments at higher dynamic pressure (i.e., later in the observation span) had more measurement points because they were easier to detect after the main flares had ended. Estimation theory tells us that the uncertainty should tend to decrease if more measurements are available. It is difficult to draw conclusions on the main spacecraft's estimated β_D and β_L early in the reentry; there is high uncertainty in the EKF's estimates of these states at low dynamic pressure, and preflight predicted values also have high uncertainty because the spacecraft is expected to begin tumbling soon after reentry. Another apparent trend in Fig. 10 is that fragments with high area-to-mass ratio (reflected in β_D) are more likely to break off earlier (e.g., solar panels).

Because the fragments have low β_L/β_D, one can assume that they have simple spherical shapes to approximate their mass and size (and also to analyze their ablation coefficients, see Sec. VI). The radius and mass are calculated for two assumed shapes: a solid sphere and a spherical shell having thickness 0.1 times the outer radius. For both cases, $C_D = 1$ and the material is assumed to be aluminum. The range of calculated mass and radius is shown in Fig. 13 over a domain of input β_D. Comparing the results of Fig. 13 with the estimated β_D (Fig. 10), the observed fragments would each have a radius on the order of millimeters or centimeters, and mass on the order of grams. This result supports JAXA's preflight prediction that the spacecraft would be entirely consumed during reentry with low probability of large fragments surviving to impact.

It is important to note that Figs. 10 and 11 may be biases of the observation system that was operated to track the capsule. Objects that are more "cannonball-like" (i.e., low β_D) will have less deceleration, so that, toward the end of the observation span, it is more likely that objects that appear closer to the capsule in the along-track direction will be observed (recall Fig. 1). Along similar reasoning, in the beginning of the measurement span, objects with high area-to-mass (i.e., high β_D) are more likely to be observed because they are the ones that deviate from the main fireball (i.e., objects closer to the main fireball are obscured). Thus, this analysis may be useful for future studies or observation system designs because it gives insight into the probability of observing different kinds of fragments during spacecraft disintegration.

Although this study does not focus on the trajectory estimation of the capsule because such results have been previously published elsewhere [3], the capsule can serve as a useful check of this system's ability to estimate β_D and β_L. The capsule's mass ($m = 17$ kg) and cross-sectional area ($S = 0.128$ m^2) are well known, and it likely had a near-nominal reentry for several reasons (e.g., estimated trajectory matching within 2 km of nominal [3]). The predicted values of C_D and C_L depend on the Mach number and attitude motion of the capsule [52]. Approximate values of $C_D = 1.1$ and $C_L = 0$ are used here for the purposes of this check, resulting in nominal values of $\beta_D = 8 \times 10^{-3}$ and $\beta_L = 0$ m^2/kg. The EKF and batch initialization are run with the same settings as described in Sec. IV.D, with the capsule's β_D and β_L estimation results shown in Fig. 14. It is clear that the EKF's estimated values converge closely to the nominal values after approximately 5 s. Although some of the debris fragments have a shorter measurement span, this result gives additional confidence in

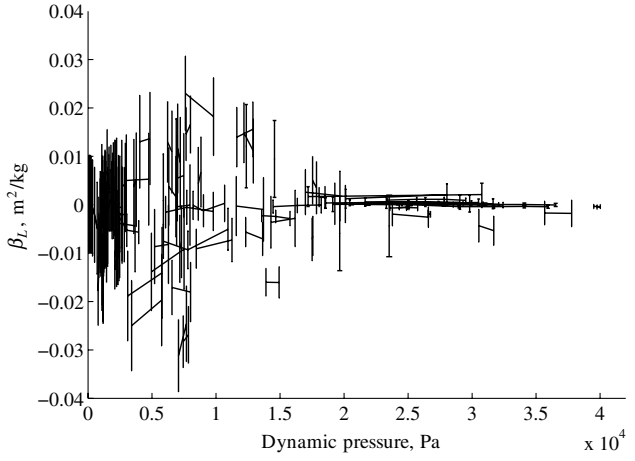

Fig. 11 Estimated lift ballistic coefficient versus freestream dynamic pressure (with 1-σ uncertainties). Uncertainty in the calculated dynamic pressure is ignored in this plot.

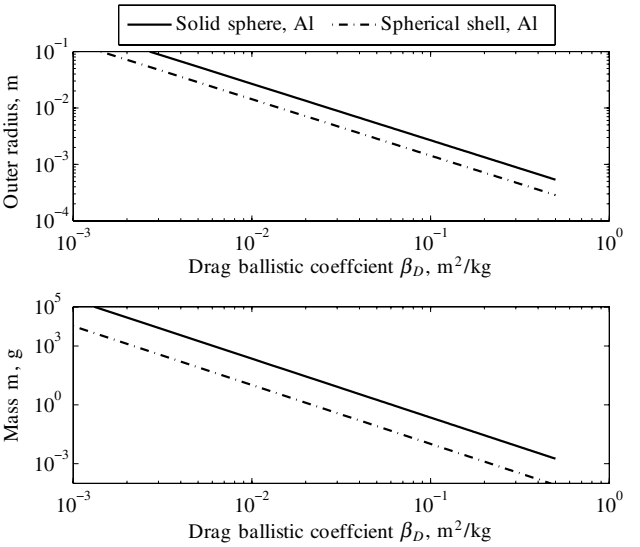

Fig. 13 Theoretical fragment radius and mass, assuming aluminum spheres.

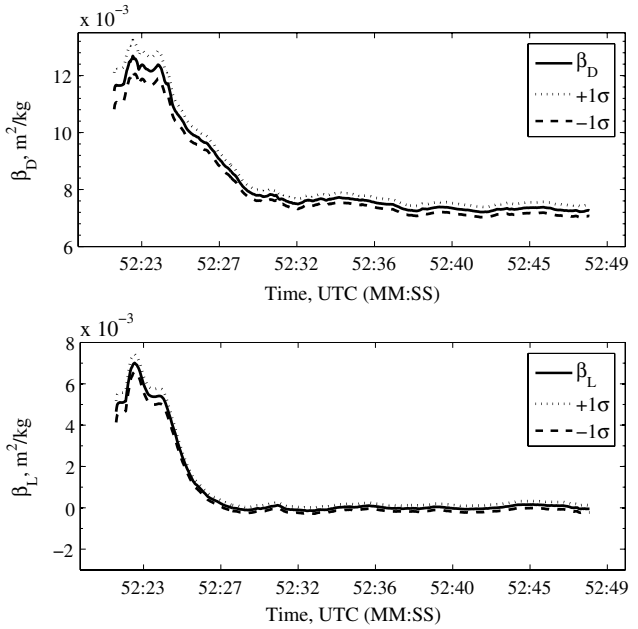

Fig. 14 Estimated β_D and β_L for the capsule.

this estimator's results, especially for those fragments having long measurement spans at the end of the reentry.

VI. Ablation Coefficient

Mass loss by ablation is one of the dynamic equations often used to solve for the trajectory and physical parameters of a meteor [40–42]. A well-known result is that, by dividing the scalar deceleration equation with the scalar mass-loss equation, one obtains

$$\frac{\mathrm{d}m}{\mathrm{d}t} = \varsigma m v_{\mathrm{er}} \frac{\mathrm{d}v_{\mathrm{er}}}{\mathrm{d}t} \tag{36}$$

The ablation coefficient is defined as $\varsigma \equiv C_H/(C_D\xi)$, and here the symbol ς is used instead of σ (which is commonly used by meteor researchers) to avoid confusion with the standard deviation. The heat of ablation ξ depends on the body's material properties and type of ablation (e.g., vaporization, liquid runoff). The coefficients C_D and C_H depend on the body configuration and aerodynamic flow regime (e.g., rarefied, continuum).

The physics of meteor reentry commonly assume (e.g., [36] p. 6) that 1) the rate of heat radiation from the body is small compared with the total heat input rate, and 2) the rate of heat storage within the body is negligible compared with the total heat input rate. The first assumption is valid for all but very small particles at high speed (e.g., dust-sized meteors). The second assumption is valid when the thermal conductivity of the body is low. Because this theory and the associated trajectory estimation methods [i.e., derived from Eq. (36)] have been successfully applied to a range of stony and ferrous meteors (including recovered kilogram-sized meteorites [51,53–55]), this paper assumes that the heating assumptions can also be applied to the fragments of the Hayabusa spacecraft.

Integrating Eq. (36) from t_0 to t_f, one obtains

$$\exp\{\varsigma[v_{\mathrm{er}}^2(t_f) - v_{\mathrm{er}}^2(t_0)]/2\} = m(t_f)/m(t_0) \tag{37}$$

where ς is assumed constant over the limits of integration. It is straightforward to show, using the definition of β_D, that

$$m(t_f)/m(t_0) = [\beta_D(t_0)/\beta_D(t_f)]^3 \tag{38}$$

for reentry bodies having time-invariant material density and shape (e.g., a sphere remains a sphere). Thus, given the initial and final values of v_{er} and β, one can solve for ς by substituting Eq. (38) into Eq. (37) and rearranging

$$\varsigma = 6\ \ln[\beta_D(t_0)/\beta_D(t_f)]/[v_{\mathrm{er}}^2(t_f) - v_{\mathrm{er}}^2(t_0)] \tag{39}$$

where a solution for ς exists if $\beta_D(t_0)/\beta_D(t_f) > 0$ and $v_{\mathrm{er}}(t_f) \neq v_{\mathrm{er}}(t_0)$. Given the expected case, in which the reentry body decelerates [i.e., $v_{\mathrm{er}}(t_f) < v_{\mathrm{er}}(t_0)$], then $\ln[\beta_D(t_0)/\beta_D(t_f)]$ must be negative for ς to be positive (and hence physically meaningful). Therefore, because the EKF's estimated β_D is allowed to increase or decrease as a result of being modeled as a random walk, the ablation coefficient analysis must be restricted to cases in which $\beta_D(t_0) < \beta_D(t_f)$. For a reentry fragment satisfying this restriction, the average ς over the measurement span is calculated by setting t_0 and t_f to that fragment's initial and final data points, respectively. Because the derivation of Eq. (37) assumes nonlifting reentry dynamics, only fragments with $\beta_L/\beta_D < 0.1$ (i.e., those that are approximately nonlifting) are used to calculate ς.

Figure 15 shows the calculated ablation coefficients, and two reference lines representing the approximate maximum values for iron and aluminum serve as a check. These two elements are used as a check because of their presence in the spacecraft structure. The upper limit of ς is found with ξ corresponding to the heat of fusion of the element. The maximum value for C_H/C_D for a sphere is 0.5, regardless of the flow regime or type of heating (i.e., purely convective or purely gas-cap radiation) [36]. It is more difficult to determine a lower limit for ς because the body's ablation may include some combination of vaporization and liquid runoff, which affects the choice of ξ and C_H. Figure 15 shows that the calculated ς are reasonable because they almost entirely fall below the theoretical maximum. The calculated ς values in this study agree with those given in [33], which used multiple ground-based long-exposure cameras to estimate ablation coefficients of 7×10^{-8} and 1×10^{-6} s^2/m^2 for two Hayabusa fragments using other trajectory estimation methods. The values of ς for the Hayabusa fragments are also similar to those for several meteors given in the literature: 3×10^{-9} s^2/m^2 [51], 1×10^{-8} s^2/m^2 [53], and 2×10^{-8} s^2/m^2 [54]. The ablation coefficients shown in Fig. 15, which are well below the theoretical maximum, suggest that the ablation occurred due to melting and evaporation of the material surface [51].

There are other possible approaches to analyzing the ablation of a reentering body that were not considered in this study. Meteor researchers often relate the measured brightness of a meteor to its mass loss and deceleration (e.g., [56], pp. 361–370), with one such relation being

$$I = -\tau_{\mathrm{lum}}\left(1 + \frac{2}{\varsigma v_{\mathrm{er}}^2}\right)\frac{v_{\mathrm{er}}^2}{2}\frac{\mathrm{d}m}{\mathrm{d}t} \tag{40}$$

where I is the meteor luminosity and τ_{lum} is the dimensionless luminous efficiency. However, one difficulty of this approach involves

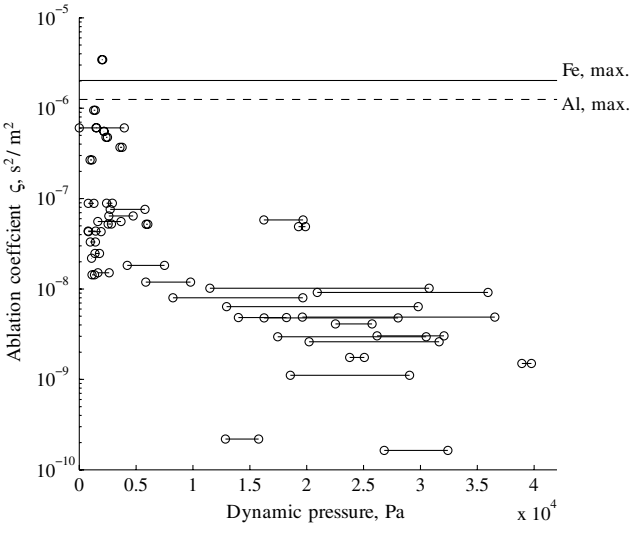

Fig. 15 Ablation coefficients.

the proper choice of τ_{lum}; this parameter is variable and depends on the spectral region of observations, chemical composition of the meteoroid and the atmosphere, and the meteoroid velocity and mass.

If the surface temperatures of the body can be measured, this information can be used to validate ablation models (assuming one also has knowledge of the body's material properties and aerodynamic flow conditions). Although the space shuttle orbiter does not use an ablative thermal protection system, [57–59] are examples of using infrared and near-infrared thermal imaging of the reentering orbiter to validate boundary-layer transition and turbulent heating prediction methods. Airborne spectral observations of the reentering Stardust capsule were used to assess the surface temperatures, which were then compared with computational fluid dynamics simulations and material response predictions of its ablative heat shield [60–63]. Similar airborne [64–66] and ground-based [49] spectral observations and surface temperature analyses were performed on the Hayabusa capsule. However, it would be challenging to apply these methods to the ablation analysis of the main spacecraft fragments; in addition to the uncertainty in the material properties and flow conditions, it may be difficult to achieve the necessary spatial resolution of the spectral emissions or to distinguish between wake and surface effects.

VII. Conclusions

An extended Kalman filter with batch initialization is used to estimate the position, velocity, and drag and lift ballistic coefficients of the Hayabusa main spacecraft and fragments during destructive atmospheric reentry. This study makes contributions by providing trajectory estimation data on spacecraft atmospheric disposal, which is often difficult to obtain. The ground-based video observations used in this study were also unique because they captured a large number of fragments against the clear night sky, of which 80 individual fragments were analyzed.

The main spacecraft disintegration begins around 70 km altitude and ends at approximately 60 km altitude. Some fragments are observed early during the disintegration, but most fragments are measurable after the main disintegration (and after maximum dynamic pressure). The first observed fragment is suspected to be a solar panel, because it has high area-to-mass ratio and its time of separation matches within several seconds with the preflight predictions. Almost all fragments are estimated to have drag forces several orders of magnitude larger than their lift forces, which validates ballistic modeling. Assuming simple spherical shapes shows that the observed fragments would have radius and mass on the order of centimeters and grams, respectively, supporting the preflight prediction that the spacecraft fragments would have low probability of survival to impact. Objects with lower drag ballistic coefficients are more likely to be observed later during the reentry, but this may be partially due to the measurement system operation. Estimated ablation coefficients for the fragments were lower than the theoretical maximum and suggest that the fragments were ablating due to surface melting and evaporation.

Acknowledgments

This work was possible thanks to all of the Japan Aerospace Exploration Agency personnel who organized and participated in the Hayabusa recovery operations, especially Jun'ichiro Kawaguchi, Hitoshi Kuninaka, and Tetsuya Yamada. We also thank Shinji Hokamoto and Shigeru Aso of Kyushu University for providing feedback on an early draft of this paper.

References

[1] Fujita, K., Yamamoto, M., Abe, S., Ishihara, Y., Iiyama, O., Kakinami, Y., Hiramatsu, Y., Furumoto, M., Takayanagi, H., Suzuki, T., Yanagisawa, T., Kurosaki, H., Shoemaker, M., Ueda, M., Shiba, Y., and Suzuki, M., "An Overview of JAXA's Ground-Observation Activities for HAYABUSA Reentry," *Publications of the Astronomical Society of Japan*, Vol. 63, 2011, pp. 961–969.

[2] Grinstead, J., Jenniskens, P., Cassell, A., Albers, J., and Winters, M., "Airborne Observation of the Hayabusa Sample Return Capsule Reentry," AIAA Paper 2011-3329, 2011.

[3] Shoemaker, M., van der Ha, J., and Fujita, K., "Trajectory Reconstruction of Hayabusa's Atmospheric Reentry," *Acta Astronautica*, Vol. 71, 2012, pp. 151–162. doi:10.1016/j.actaastro.2011.08.006

[4] Mrozinski, R., Mendeck, G., and Cutri-Kohart, R., "Overview of Entry Risk Predictions," *Advances in Space Research*, Vol. 34, No. 5, 2004, pp. 1044–1048. doi:10.1016/j.asr.2003.02.038

[5] Bouslog, S., Ross, B., and Madden, C., "Space Debris Reentry Risk Analysis," AIAA Paper 1994-0591, 1994.

[6] O'Hara, R., and Johnson, N., "Reentry Survivability Risk Assessment of the Extreme Ultraviolet Explorer (EUVE)," *Proceedings of the Third European Conference on Space Debris*, Darmstadt, Germany, 2001; also ESA Paper SP-473.

[7] Rochelle, W., Marichalar, J., and Johnson, N., "Analysis of Reentry Survivability of UARS Spacecraft," *Advances in Space Research*, Vol. 34, 2004, pp. 1049–1054. doi:10.1016/j.asr.2003.01.011

[8] Smith, R., Bledsoe, K., Dobarco-Otero, J., Rochelle, W., Johnson, N., Pergosky, A., and Weiss, M., "Reentry Survivability Analysis of the Hubble Space Telescope (HST)," *Proceedings of the Fourth European Conference on Space Debris*, Darmstadt, Germany, Aug. 2005; also ESA Paper SP-587.

[9] Salama, A., Ling, L., and McRonald, A., "A Genesis Breakup and Burnup Analysis in Off-Nominal Earth Return and Atmospheric Entry," *Advances in the Astronautical Sciences*, Vol. 123, edited by Williams, B., D'Amario, L., Howell, K., and Hoots, F., Univelt, San Diego, CA, pp. 2155–2170, 2005.

[10] Klinkrad, H., Fritsche, B., and Kashkovsky, A., "Prediction of Spacecraft Destruction During Uncontrolled Re-Entries," *Proceedings of the European Conference on Spacecraft Structures, Materials and Mechanical Testing*, Noordwijk, The Netherlands, 2001; also ESA Paper SP-468.

[11] Lips, T., Fritsche, B., Koppenwallner, G., and Klinkrad, H., "Spacecraft Destruction During Re-Entry—Latest Results and Development of the SCARAB Software System," *Advances in Space Research*, Vol. 34, 2004, pp. 1055–1060. doi:10.1016/j.asr.2003.01.012

[12] Fritsche, B., Lips, T., and Koppenwallner, G., "Analytical and Numerical Re-Entry of Simple-Shaped Objects," *Acta Astronautica*, Vol. 60, 2007, pp. 737–751. doi:10.1016/j.actaastro.2006.07.017

[13] Tewari, A., "Entry Trajectory Model with Thermomechanical Breakup," *Journal of Spacecraft and Rockets*, Vol. 46, No. 2, 2009, pp. 299–306. doi:10.2514/1.39651

[14] Weaver, M., Baker, R., and Frank, M., "Probabilistic Estimation of Reentry Debris Area," *Proceedings of the Third European Conference on Space Debris*, Darmstadt, Germany, 2001; also ESA Paper SP-473.

[15] Frank, M., Weaver, M., and Baker, R., "A Probabilistic Paradigm for Spacecraft Random Reentry Disassembly," *Reliability Engineering and System Safety*, Vol. 90, Nos. 2–3, 2005, pp. 148–161. doi:10.1016/j.ress.2004.10.013

[16] Wilson, S., Vuletich, I., Bryce, I., Brett, M., Williams, W., Fletcher, D., Jokic, M., and Cooper, N., "Space Launch and Re-Entry Risk Hazard Analysis—A New Capability," *Proceedings of the 60th International Astronautical Congress*, International Astronautical Federation, Daejeon, Republic of Korea, 2009; also IAC Paper 09-D2.2.09.

[17] Brett, M., Wilson, S., Vuletich, I., Tisato, J., Williams, W., and Guthrie, P., "Risk Hazard Analysis for Commercial Spaceflight Activities Using Range Safety Template Toolkit," *Proceedings of the 62th International Astronautical Congress*, International Astronautical Federation, Cape Town, South Africa, 2011; also IAC Paper 11-D6.1.2

[18] Patera, R., and Ailor, W., "The Realities of Reentry Disposal," *Advances in the Astronautical Sciences*, Vol. 99, edited by Middour, J., Sackett, L., D'Amario, L., and Byrnes, D., Univelt, San Diego, CA, pp. 1059–1071, 1998.

[19] Ailor, W., Bywater, R., and Gurevich, L., "Spacecraft Reentry Breakup Recorder," U.S. Patent US 6,895,314 B2, 2005.

[20] Ailor, W., Dupzyk, I., Shepard, J., and Newfield, M., "REBR: An Innovative, Cost-Effective System for Return of Reentry Data," AIAA Paper 2007-6222, 2007.

[21] Lips, T., and Fritsche, B., "A Comparison of Commonly Used Re-Entry Analysis Tools," *Acta Astronautica*, Vol. 57, 2005, pp. 312–323. doi:10.1016/j.actaastro.2005.03.010

[22] Lips, T., Wartemann, V., Koppenwallner, G., Klinkrad, H., Alwes, D., Dobarco-Otero, J., Smith, R., DeLaune, R., Rochelle, W., and Johnson, N., "Comparison of ORSAT and SCARAB Reentry Survival Results," *Proceedings of the Fourth European Conference on Space Debris*, Darmstadt, Germany, 2005; also ESA Paper SP-587.

[23] "Nuclear Safety Research and Development Program—Summary Report," U.S. Atomic Energy Commission TR WASH-1052, 1964.
[24] Parsons, D., "Reentry Flight Demonstration Number Two (RFD-2): Spectrographs, Photometers, and Event Cameras Developed for SNAP Reentry Studies," Sandia Corp. TR SC-RR-64-968, Albuquerque, NM, 1964.
[25] *Columbia Crew Survival Investigation Report*, NASA NASA/SP-2008-565, 2009, p. 19, Chap. 4.
[26] *Columbia Accident Investigation Board Report*, NASA PB2004-100868, Vol. 3, 2003, pp. 213–287.
[27] Giannopapa, C., Hatton, J., Franken, E., van der Linden, B., and Jenniskens, P., "High Speed Imaging of the Fragmentation of the Jules Verne Automated Transfer Vehicle," *Proceedings of the ASME 2009 Pressure Vessels and Piping Division Conference*, American Society of Mechanical Engineers, Fairfield, NJ, 2009, pp. 599–604.
[28] De Pasquale, E., Francillout, L., Wasbauer, J., Hatton, J., Albers, J., and Steele, D., "ATV Jules Verne Reentry Observation: Mission Design and Trajectory Analysis," *IEEE Aerospace Conference 2009*, Inst. of Electrical and Electronics Engineer Paper 1155, 2009.
[29] Jenniskens, P., Wercinski, P., Olejniczak, J., Wright, M., Raiche, G., Kontinos, D., Desai, P., Spalding, R., Sandquist, K., Rossano, G., Russell, R., Revelle, D., Hladiuk, D., and Hildebrand, A., "Surface Heating from Remote Sensing of the Hypervelocity Entry of the NASA GENESIS Sample Return Capsule," AIAA Paper 2006-381, 2006.
[30] Kontinos, D., and Wright, M., "Introduction: Atmospheric Entry of the Stardust Sample Return Capsule," *Journal of Spacecraft and Rockets*, Vol. 47, No. 6, 2010, pp. 865–867. doi:10.2514/1.52887
[31] Rao, A., "Minimum-Variance Estimation of Reentry Debris Trajectories," *Journal of Spacecraft and Rockets*, Vol. 37, No. 3, 2000, pp. 366–373. doi:10.2514/2.3570
[32] Tardy, J., and Kluever, C., "Estimation and Prediction of Orbital Debris Reentry Trajectories," *Journal of Spacecraft and Rockets*, Vol. 39, No. 6, 2002, pp. 845–851. doi:10.2514/2.3906
[33] Borovicka, J., Abe, S., Shrbený, L., Spurný, P., and Bland, P., "Photographic and Radiometric Observations of the HAYABUSA Reentry," *Publications of the Astronomical Society of Japan*, Vol. 63, 2011, pp. 1003–1009.
[34] Watanabe, J., Ohkawa, T., Sato, M., Ohnishi, K., and Iijima, Y., "Fragmentation of the HAYABUSA Spacecraft on Re-Entry," *Publications of the Astronomical Society of Japan*, Vol. 63, 2011, pp. 955–960.
[35] Riddell, F., and Winkler, H., "Meteorites and Re-Entry of Space Vehicles at Meteor Velocities," *ARS Journal*, Vol. 32, No. 10, 1962, pp. 1523–1530. doi:10.2514/8.6324
[36] Allen, H., and James, N., "Prospects for Obtaining Aerodynamic Heating Results From Analysis of Meteor Flight Data," NASA TR TN D-2069, 1964.
[37] Fay, J., Moffatt, W., and Probstein, R., "An Analytical Study of Meteor Entry," *AIAA Journal*, Vol. 2, No. 5, 1964, pp. 845–854.
[38] Allen, H., Baldwin, B. Jr., and James, N., "Effect on Meteor Flight of Cooling by Radiation and Ablation," NASA TR TN D-2872, 1965.
[39] Romig, M., "Physics of Meteor Entry," *AIAA Journal*, Vol. 3, No. 3, 1965, pp. 385–394.
[40] Pecina, P., and Ceplecha, Z., "New Aspects in Single-Body Meteor Physics," *Bulletin of the Astronomical Institutes of Czechoslovakia*, Vol. 34, 1983, pp. 102–121.
[41] Ceplecha, Z., "Geometric, Dynamic, Orbital and Photometric Data on Meteoroids from Photographic Fireball Networks," *Bulletin of the Astronomical Institutes of Czechoslovakia*, Vol. 38, No. 4, 1987, pp. 222–234.
[42] Borovička, J., "The Comparison of Two Methods of Determining Meteor Trajectories From Photographs," *Bulletin of the Astronomical Institutes of Czechoslovakia*, Vol. 41, No. 6, 1990, pp. 391–396.
[43] Vallado, D., *Fundamentals of Astrodynamics and Applications*, 2nd ed., Microcosm Press, El Segundo, CA, 2004.
[44] Crassidis, J., and Junkins, J., *Optimal Estimation of Dynamic Systems*, Chapman and Hall, Washington, DC, 2004, pp. 283–292.
[45] Hough, M., "Improved Performance of Recursive Tracking Filters Using Batch Initialization and Process Noise Adaptation," *Journal of Guidance, Control, and Dynamics*, Vol. 22, No. 5, 1999, pp. 675–681. doi:10.2514/2.4457
[46] Hough, M., "Nonlinear Recursive Estimation of Boost Trajectories, Including Batch Initialization and Burnout Estimation," *Journal of Guidance, Control, and Dynamics*, Vol. 29, No. 1, 2006, pp. 72–81. doi:10.2514/1.13135
[47] Tapley, B., Schutz, B., and Born, G., *Statistical Orbit Determination*, Elsevier, New York, 2004, pp. 194–199, Chap. 4.
[48] Shuster, M., "Kalman Filtering of Spacecraft Attitude and the QUEST Model," *Journal of the Astronautical Sciences*, Vol. 38, No. 3, 1990, pp. 377–393.
[49] Abe, S., Fujita, K., Kakinami, Y., Iiyama, O., Kurosaki, H., Shoemaker, M., Shiba, Y., Ueda, M., and Suzuki, M., "Near-Ultraviolet and Visible Spectroscopy of HAYABUSA Spacecraft Re-Entry," *Publications of the Astronomical Society of Japan*, Vol. 63, 2011, pp. 1011–1021.
[50] Luchinski, V., Murtazin, R., Sytin, O., and Ulybyshev, Y., "Mission Profile of Targeted Splashdown for Space Station Mir," *Journal of Spacecraft and Rockets*, Vol. 40, No. 5, 2003, pp. 665–671. doi:10.2514/2.6915
[51] Borovička, J., and Kalenda, P., "The Morávka Meteorite Fall: 4. Meteoroid Dynamics and Fragmentation in the Atmosphere," *Meteorics and Planetary Science*, Vol. 38, No. 7, 2003, pp. 1023–1043.
[52] Ishii, N., Yamada, T., Hiraki, K., and Inatani, Y., "Reentry Motion and Aerodynamics of the MUSES-C Sample Return Capsule," *Transactions of the Japan Society for Aeronautical and Space Sciences*, Vol. 51, No. 172, 2008, pp. 65–70. doi:10.2322/tjsass.51.65
[53] Ceplecha, Z., "Luminous Efficiency Based on Photographic Observations of the Lost City Fireball and Implications for the Influx of Interplanetary Bodies onto Earth," *Astronomy and Astrophysics*, Vol. 311, 1996, pp. 329–332.
[54] Spurný, P., Heinlein, D., and Oberst, J., "The Atmospheric Trajectory and Heliocentric Orbit of the Neuschwanstein Meteorite Fall on April 6, 2002," *Proceedings of Asteroids, Comets, Meteors — ACM 2002*, Warmbein, B. ed., Noordwijk, The Netherlands, 2002, pp. 137–140; also ESA Paper SP-500.
[55] Spurný, P., Oberst, J., and Heinlein, D., "Photographic Observations of Neuschwanstein, a Second Meteorite from the Orbit of the Příbram chondrite," *Nature*, Vol. 423, 2003, pp. 151–153.
[56] Ceplecha, Z., Borovička, J., Elford, W., Revelle, D., Hawkes, R., Porubčan, V., and Šimek, M., "Meteor Phenomena and Bodies," *Space Science Reviews*, Vol. 84, 1998, pp. 327–471. doi:10.1023/A:1005069928850
[57] Blanchard, R., Wilmoth, R., Glass, C., Merski, N., Berry, S., Bozung, T., Tietjen, A., Wendt, J., and Dawson, D., "Infrared Sensing Aeroheating Flight Experiment: STS-96 Flight Results," *Journal of Spacecraft and Rockets*, Vol. 38, 2001, pp. 465–472. doi:10.2514/2.3713
[58] Zalameda, J., Horvath, T., Tomek, D., Tietjen, A., Gibson, D., Mercer, D., Shea, E., Bush, B., Tack, S., and Taylor, J., "Application of a Near Infrared Imaging System for Thermographic Imaging of the Space Shuttle During Hypersonic Re-Entry," *Proceedings of 48th AIAA Aerospace Sciences Meeting and Exhibit*, Orlando, Florida, AIAA Paper 2010-245, 2010.
[59] Spisz, T., Taylor, J., Kennerly, S., Osei-Wusu, K., Gibson, D., Horvath, T., Zalameda, J, Kerns, R., Shea, E., Mercer, C., Schwartz, R., Dantowitz, R., and Kozubal, R., "Processing Ground-Based Near-Infrared Imagery of Space Shuttle Re-Entries," *Proceedings SPIE 8354, Thermosense: Thermal Infrared Applications XXXIV*, 2012, p. 83540G. doi:10.1117/12.919232
[60] Jenniskens, P., "Observations of the Stardust Sample Return Capsule Entry with a Slitless Echelle Spectrograph," *Journal of Spacecraft and Rockets*, Vol. 47, No. 5, 2010, pp. 718–735. doi:10.2514/1.37518
[61] Jenniskens, P., Koop, M., and Albers, J., "Intensified Low-Resolution Optical Spectroscopy of the Stardust Sample Return Capsule Entry," *Journal of Spacecraft and Rockets*, Vol. 47, No. 6, 2010, pp. 895–900.
[62] Trumble, K., Cozmuta, I., Sepka, S., Jenniskens, P., and Winter, M., "Postflight Aerothermal Analysis of Stardust Sample Return Capsule," *Journal of Spacecraft and Rockets*, Vol. 47, No. 5, 2010, pp. 765–774. doi:10.2514/1.41514
[63] Winter, M., and Trumble, K., "Near-Ultraviolet Emission Spectroscopy During an Airborne Observation of the Stardust Reentry," *Journal of Spacecraft and Rockets*, Vol. 48, No. 1, 2011, pp. 59–71. doi:10.2514/1.38176
[64] Buttsworth, D., Morgan, R., and Jenniskens, P., "Near Ultraviolet Emission Spectroscopy of the Hayabusa Re-Entry," AIAA Paper 2012-1297, 2012.
[65] Jenniskens, P., Kozubal, M., Dantowitz, R., Breitmeyer, J., Winter, M., Grinstead, J., and Loehle, S., "Time-Resolved Absolute Irradiance of the Hayabusa Sample Return Reentry," AIAA Paper 2012-1294, 2012.
[66] Rairden, R., and Jenniskens, P., "Intensified Near-UV Spectroscopy of the Hayabusa Reentry," AIAA Paper 2012-1280, 2012.

C. Kluever
Associate Editor